APPLIED SCIENCES AND ENGINEERING

A wireless, solar-powered, optoelectronic system for spatial restriction-free long-term optogenetic neuromodulations

Jaejin Park[1]†, Kyubeen Kim[1]†, Yujin Kim[2]†, Tae Soo Kim[1,3]†, In Sik Min[1], Bowen Li[4], Young Uk Cho[1], Chanwoo Lee[1], Ju Young Lee[1], Yuyan Gao[4], Kyowon Kang[1], Do Hyeon Kim[5], Won Jun Choi[3], Hyun-Beom Shin[6], Ho Kwan Kang[6], Young Min Song[5], Huanyu Cheng[4,7], Il-Joo Cho[2,8]*, Ki Jun Yu[1,9]*

Numerous wireless optogenetic systems have been reported for practical tether-free optogenetics in freely moving animals. However, most devices rely on battery-powered or coil-powered systems requiring periodic battery replacement or bulky, high-cost charging equipment with delicate antenna design. This leads to spatiotemporal constraints, such as limited experimental duration due to battery life or animals' restricted movement within specific areas to maintain wireless power transmission. In this study, we present a wireless, solar-powered, flexible optoelectronic device for neuromodulation of the complete freely behaving subject. This device provides chronic operation without battery replacement or other external settings including impedance matching technique and radio frequency generators. Our device uses high-efficiency, thin InGaP/GaAs tandem flexible photovoltaics to harvest energy from various light sources, which powers Bluetooth system to facilitate long-term, on-demand use. Observation of sustained locomotion behaviors for a month in mice via secondary motor cortex area stimulation demonstrates the notable capabilities of our device, highlighting its potential for space-free neuromodulating applications.

INTRODUCTION

The understanding and manipulation of brain circuits have long been a challenge for neuroscientists due to their remarkable complexity. Optogenetics is an emerging research tool that combines the principles of genetics and optics to enable precise control of neuronal activity, offering a groundbreaking approach to investigating brain circuits (*1*, *2*). This technique substantially advanced our understanding of the nervous system by providing an unprecedented level of resolution for manipulating and monitoring the activity of specific target neural circuits and presented potential therapeutic applications for brain disorders and neurodegenerative diseases (*3*–*6*). Overcoming the limitations of conventional optogenetic approaches like tethered and wired light delivery (*3*, *7*, *8*) is crucial to effectively study brain circuits under undisturbed naturalistic behavior. These tethered systems with bulky optical wires substantially restrict animals′ movement, impede their natural behavior, and limit the scope of experimental paradigms that can be used, such as complex behavior tests, social interactions, prolonged tasks, and multiple animals′ in vivo experiments.

Recent advancements in optogenetics have incorporated wireless systems, enabling individualized applications for each subject and overcoming the limitations of tethered approaches by allowing control of neuronal activities for freely moving animals. However, wireless optogenetic technologies, including battery-operated (*9*–*14*) and coil-used radio frequency (rf) power transfer systems (*15*–*22*), face challenges related to power supply strategies for continuous operation. Battery-operated systems require periodic battery replacements, which not only complicate the conduct of long-term studies but also induce stress in the animals and prevent them from being in a natural state. Most rechargeable battery systems frequently require animals to be restricted in a designated area while undergoing the recharging procedure. Coil-powered systems, on the other hand, need intricate designs for transmitting and receiving antennas, limiting their operation to a confined cage space due to the cage-wrapping coil antenna design. The power transfer efficiency of coil-powered systems is heavily dependent on antenna design. Any modifications in the coil angles due to the movement of the target can significantly affect the antenna's sensitivity, resulting in reduced power transfer efficiency and disruptions in signal transmission (*19*, *23*). To mitigate these issues and ensure smooth operation within the cage, optogenetic electronics often incorporate supercapacitors in the circuit of implant devices as well as use costly and bulky equipment like rf amplifiers and function generators. The practical implementation of these devices also requires advanced technical expertise, such as impedance matching, which can be challenging. Although

[1]Functional Bio-integrated Electronics and Energy Management Lab, School of Electrical and Electronic Engineering, Yonsei University, 50 Yonsei-ro, Seodaemun-gu, Seoul 03722, Republic of Korea. [2]Department of Biomedical Sciences, College of Medicine, Korea University, 73 Goryeodae-ro, Seongbuk-gu, Seoul 02841, Republic of Korea. [3]Center for Opto-Electronic Materials and Devices, Korea Institute of Science and Technology (KIST), Seoul 02792, Korea. [4]Department of Engineering Science and Mechanics, The Pennsylvania State University, University Park, PA 16802, USA. [5]School of Electrical Engineering and Computer Science (EECS), Gwangju Institute of Science and Technology (GIST), Gwangju 61005, Republic of Korea. [6]Korea Advanced Nano Fab Center (KANC), Suwon 443-270, Korea. [7]Materials Research Institute, The Pennsylvania State University, University Park, PA 16802, USA. [8]Department of Anatomy, College of Medicine, Korea University, 73 Goryeodae-ro, Seongbuk-gu, Seoul 02841, Republic of Korea. [9]Department of Electrical and Electronic Engineering, YU-Korea Institute of Science and Technology (KIST) Institute, Yonsei University, 50, Yonsei-ro, Seodaemun-gu, Seoul 03722, Korea.
*Corresponding author. Email: kijunyu@yonsei.ac.kr (K.J.Y.); ijcho@korea.ac.kr (I.-J.C.)
†These authors contributed equally to this work.

some attempts have been made to use photovoltaics (PV) as a power source for optogenetic devices (*24*, *25*), these implementations have either limited the animals' freely moving behavior due to the use of anesthesia or merely served as supplementary power sources alongside rf coils. Various materials can be used to fabricate PV energy harvesters, but their lower efficiency as power supplies presents certain limitations. For example, silicon solar cells require a relatively thick thickness to achieve high power conversion efficiency (PCE) due to their low absorption coefficient (*26*). Perovskite solar cells frequently exhibit high PCE, but the long-term reliability of the cells is still poor. In addition, organic solar cells display lower PCEs attributed to electron-hole recombination within the organic materials (*27*, *28*). Moreover, when combined with bioelectronics, perovskite and organic materials in a solar cell pose challenges related to the degradation of their performance over time and the poor minority carrier lifetime caused by their disordered and defective structures, making them less suitable as a power source for operating bioelectronics (*29*–*31*).

Those limitations have made it difficult to conduct proper investigations of the brain circuit, as current devices have not been able to eliminate the stress of the target in actual in vivo experiments and have forced them into artificial situations for operating devices. Furthermore, user-friendly device control is essential for diverse settings and sustained operation, which can be typically facilitated via smartphones. Addressing previously mentioned constraints with user-friendly device control would allow for convenient, long-term modulation without any tethering restrictions (*32*, *33*). Consequently, an alternative approach is needed to maintain the continuous long-term operation of the device without space restrictions.

To overcome the limitations of space-restricted energy-harvesting methods that necessitate bulky equipment and delicate antenna design with impedance matching, we introduce a wireless, solar-powered, flexible optoelectronics for optogenetic neuromodulation that enables long-term, reliable operation with a rechargeable design (table S1 for comparing other wireless brain optogenetic devices). For harvesting solar energy and converting it into electrical energy for wireless system operation, ultralightweight flexible InGaP/GaAs tandem solar cells are used, with a high PCE of ~18% with an area of ~1 cm^2, short circuit current (I_{sc}) of ~9.5 mA, and open circuit voltage (V_{oc}) of ~2.3 V under AM 1.5G solar spectrum. Owing to the use of III-V materials, solar cells can generate an adequate amount of power in a thin form, unlike silicon-based solar cells. With its superior absorption in broad wavelength bands, various light sources can be used as an energy supplier. For acquiring maximum energy extraction from PV, a maximum power point (MPP) tracking system is integrated to optimize performance for high output impedance dc sources, like PV, whose power varies with ambient conditions. The MPP is listed by the PV as a percentage of its open circuit voltage. The power management system also provides battery overcharging and undervoltage protection features to enhance the battery lifetime and safe use. The Bluetooth low-energy (BLE) wireless communication system fabricated on a flexible substrate is necessary for controlling neural implant devices by relieving mechanical mismatch of interfaces and meets the user's dynamic usage requirements with multiconnection. The combination of these two technologies overcomes the constraints of previously reported energy-harvesting methods that often require bulky and high-cost equipment that can only be used in confined spaces. High-efficient solar cells and the power management system enable the storage of more than a day's worth of sustainable power during daylight hours, allowing for the operation of the BLE wireless communication system even in the absence of light. This makes the device suitable for both outdoor and indoor use, and it can operate regardless of environmental factors like weather. This approach is particularly useful for neuromodulation, as, once implanted, there is no need for multiple surgeries or tethering to replace batteries, making it ideal for observing chronic neural responses in a natural long-term in vivo environment. The in vivo experiments that we conducted for a month, and the device operation scenarios demonstrate immense potential for neuroscience research.

RESULTS

Solar-powered optogenetic device overview and operational design

Progressing from past in vivo experiment systems where animals were immobilized in a stereotaxic and tethered state under anesthesia, wireless optogenetic devices have been developed, using inductive coupling and rf power transfer systems with cage-wrapped antennas. However, this approach still limits device charging and operation to the confines of a specifically equipped cage and requires additional external instruments like a function generator and rf amplifier for charging purposes. Thus, the animals must stay in the designated spaces for charging or operating the device. Meanwhile, wireless optogenetic systems with replaceable batteries can provide space unlimited optogenetics for a limited time, but the system requires frequent battery replacements for long-term neuromodulations. In addition, this battery replacement procedure can cause stress to the animals. The wireless solar-powered optogenetic device (WSOD) described here, however, harnesses a light energy harvester for power supply, eliminating spatial constraints (Fig. 1A and movie S1). The device can operate in any experimental setting and environment, and its independence from auxiliary equipment provides a completely undisturbed state, unlike other wireless systems (*3*, *20*). Furthermore, the integrated BLE wireless communication system enables users to establish multiconnections with multiple subjects using their smartphone, providing individualized stimulation for each subject. This design allows subjects to exhibit completely natural behavior during daylight hours while concurrently storing sufficient solar energy to sustain the operation of the device, even in the absence of light.

Figure 1B presents an expanded exploded schematic illustration of WSOD before folding for miniaturization. The WSOD comprises several key components: (i) an ultralightweight, flexible PV energy harvester (cell thickness, ~5 μm) that distributes power to the entire system; (ii) a power management circuit for MPP tracking and voltage conversion; (iii) a Bluetooth system-on-chip (SoC; MBN52832) for wireless control; (iv) a lithium polymer battery (LiPo battery, 10 mAh, 8 mm by 15 mm by 2 mm) for energy storage; and (v) a microscale inorganic light-emitting diode [μ-LED, 460 nm, 210 μm (width) by 130 μm (length) by 110 μm (height)] equipped probe for mouse brain photostimulation; these components are integrated on a flexible polyimide (PI) film (~25 μm), electrically interconnected by copper traces, and subsequently encapsulated with polydimethylsiloxane (PDMS) and parylene C for device protection. The circuit diagram of the WSOD presented

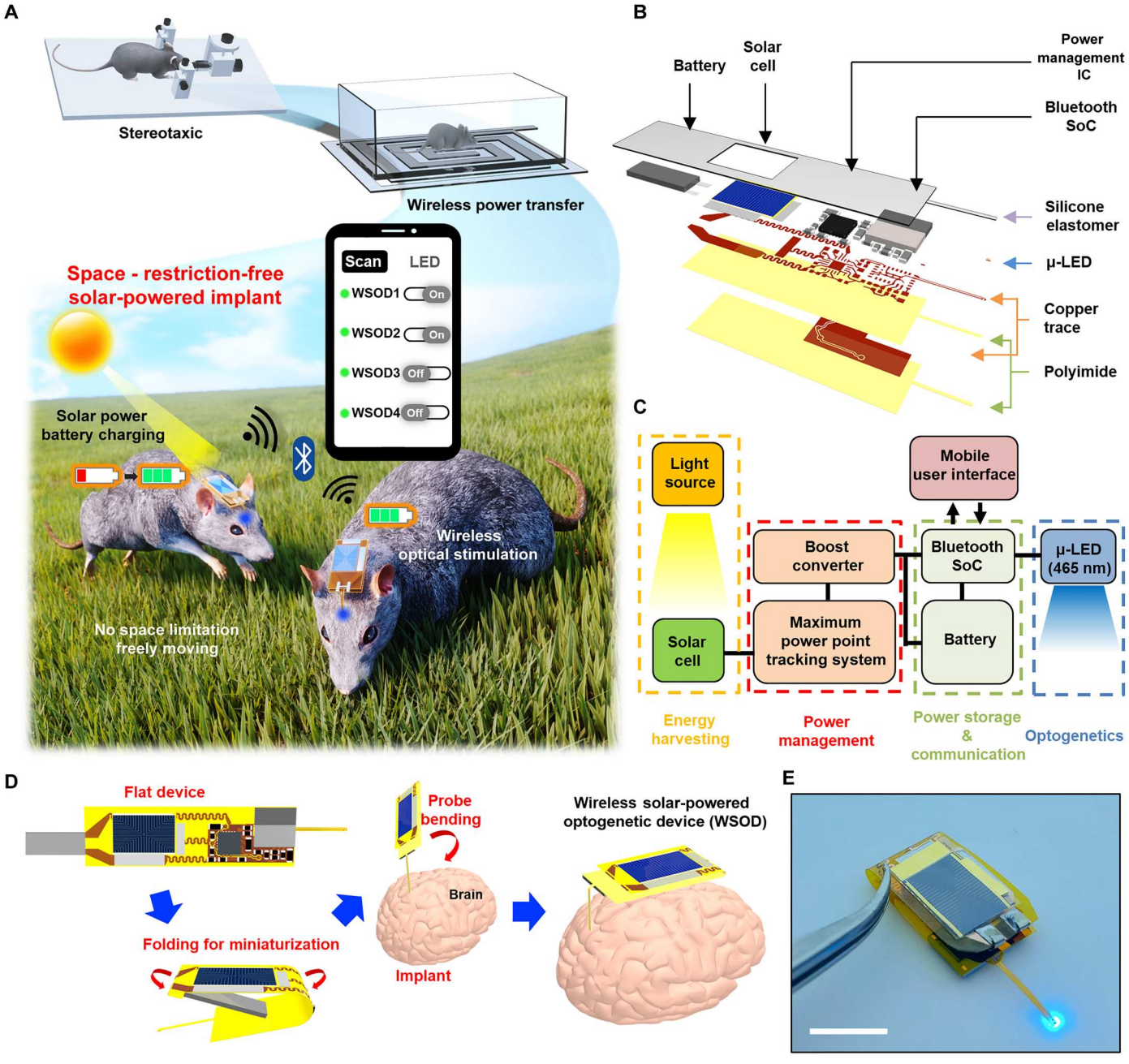

Fig. 1. Overall concept and design of the WSOD for charging and operating in wide space. (**A**) Conceptual illustration of wireless solar-powered optogenetic device (WSOD) for a completely freely moving experiment compared to conventional optogenetic device. This platform harvests solar energy and operates through Bluetooth-based wireless data communication with multiple device connections. (**B**) Layered schematic illustration of components in WSOD before miniaturization. IC, integrated circuit. (**C**) Operational block diagram of overall system design that consists of solar energy harvester, wireless rechargeable system, communication system, and micro-scale inorganic light-emitting diode (μ-LED) for photostimulation. (**D**) Flexible device folding process for miniaturization and brain implantation process of WSOD. (**E**) Optical image of WSOD with 460-nm μ-LED operation. Scale bar, 10 mm.

in Fig. 1C shows the harvested energy flow and provides a concise overview of the device operation. The InGaP/GaAs tandem solar cell features a broad permissible wavelength range (300 to 900 nm), enabling efficient power generation not only from sunlight but also from various light sources such as lamps and searchlights. The power management system, designed to control high output impedance dc sources, harvests energy at the voltage point of 80% of the solar cell's V_{oc} for maximum power efficiency. Once the charging process begins, the boost-up converter transforms the low-voltage output (~2.0 V) of the solar cell into a higher voltage (~3.7 V) for charging. The battery stores the charge while consuming only a small amount of power, sufficient to maintain a Bluetooth signal detectable by commercially supported mobile applications. In addition, when the user activates the μ-LED after connecting

Bluetooth, the operating power is drawn from the battery. The use of commercially supported mobile applications in conjunction with the BLE system provides user-friendly device operation and enhances its overall practicality. Moreover, with the adoption of customized applications, the overall systems enable multiconnection modes as well. The LiPo battery allows the Bluetooth SoC to function even in the absence of a light source for nearly 4 days without μ-LED operation (fig. S1), while its lightweight (<0.4 g) and thin (~2 mm) profile makes it suitable as a power supply for implant devices. The μ-LED neural probe, controlled by the BLE SoC′s general-purpose input/output (GPIO), can be used according to the user′s discretion and has a width of ~150 μm and a thickness of ~100 μm. As reported in previous studies, these dimensions are similar to other optoelectronic probes applicable to brain tissue, allowing for safe in vivo studies (*34*–*36*).

A thin flexible substrate can be folded to reduce device dimension, enabling head mount after implantation (Fig. 1D). The original flat device′s size was reduced by approximately 65% after bending the battery pad portion and the interconnect section between the solar cell and circuit board. By placing the battery between the top surface and the bottom surface, the length of the device is minimized, making it more compact and convenient for use in various experimental settings. The circuit interconnects of the folding area are designed with serpentine lines to reduce applied stress (*37*). For biofluidic shielding and mechanical buffering, the device undergoes an encapsulation process with biocompatible, soft elastomer (PDMS) and parylene C (~8 μm) for long-term device reliability, enabling nondisruptive chronic in vivo experiments. The probe is coated with polyethylene glycol and inserted into the desired target area in the brain. Then, the device body is bent, completing the transformation into a head-mounted optogenetic device. Figure 1E and fig. S2 show the view of the WSOD.

Solar cell design and electrical charging characteristics

The flexible III-V PV device (cell area, 12 mm by 8 mm) provides high energy conversion efficiency by using its high absorption over the broadband area. In addition, its mechanical flexibility makes it an optimal choice for driving flexible neuromodulation devices. Figure 2A and fig. S3 illustrate the structure of the solar cell designed for WSOD integration. The platinum/gold (Pt/Au) layer acting as bonding materials is directly deposited on a PI film (~13 μm) to create the bottom electrode and transfer the III-V materials onto the flexible substrate. Subsequently, a grid-patterned electrode is fabricated on top of this structure, serving the purpose of collecting current and thereby increasing the efficiency of the solar cell (*38*, *39*). In addition, the fabricated solar cell is encapsulated with SU-8 except for the pad area for integrating Bluetooth systems and protecting the device from the surrounding environment. Figure 2B presents the current density–voltage characteristics (J-V) of PV at room temperature under AM 1.5G illumination (1000 W/m^2). An inverted dual-junction InGaP/GaAs solar cell is grown on a 2° misoriented GaAs substrate by metal organic chemical vapor deposition. The overall epitaxy structure of the InGaP/GaAs solar cell is shown in fig. S4. The flexible InGaP/GaAs solar cell exhibits a PCE of ~18%, a V_{oc} of 2.34 V, J_{sc} of ~9.3 mA/cm^2, and a fill factor of 83%. The MPP is formed at approximately 2.1 V with a power of 18 mW/cm^2, which significantly surpasses the required power for Bluetooth operation. Figure 2C shows the measured external quantum efficiency (EQE), suggesting that the device can effectively harvest light energy from various sources, including sunlight, a lamp, and a flashlight due to its broad wavelength spectrum.

Figure 2D presents a hemispherical color mapping graph that depicts the amount of energy harvested by the WSOD-integrated solar cell in an outdoor environment at noon. The amount of harvested power is affected by the device′s tilted angle that indicates the head′s movement after implantation. During midday, the graph displays measurements taken at 10° intervals along the cardinal directions and at 15° intervals for elevation angles. As the position of the sun varies depending on the country′s latitude, longitude, and season, the actual solar altitude at the time of measurement can be found in fig. S5. The highest power obtained was approximately 15 mW when the device was inclined at around 75° from the south as a reference, almost perpendicular to the sun. At a flat state, the device obtained ~10 mW of power, and, even in the opposite direction of the sun, it harvested a minimum of 2 mW. Considering that the average power required for turning on μ-LED through BLE is under 0.6 mW over time, this suggests that the device can supply a sufficient amount of power without being affected by the changing head angles when the subject is freely moving after implantation. Figure 2E presents a graph depicting the power harvesting capabilities of the WSOD-integrated solar cell in an outdoor environment at various times of the day. The west-end of the device is lifted up from a flat state to the different angle theta so that the top faces eastward, as illustrated in the lower part of Fig. 2E. Given that the sun is at a relatively lower elevation angle at 9:00 a.m., obliquely from the ground, the device harvests more power when tilted, compared to the flat state (0°, ~6.16 mW). At 12:00 p.m., when the sun is located at the highest point compared to other times, the device maintains ~10 mW of power regardless of slight angle changes, but it receives less power at angles where sunlight does not reach easily. At 3:00 p.m., the PV cell produced less power compared to other times because the sun illuminates the backside of the solar cell. However, if inclined in the opposite direction, then the device would harvest more solar energy, implying that sufficient power for operation can be obtained like that of 9:00 a.m. at the same angle. The surface incident energy is influenced by factors such as location, climate conditions, and the incidence angle of the solar beam. To establish the reliability of the measured data, the amount of sun radiation reaching the PV (I_{nm}) is calculated by using the following formula (*40*)

$$I_{nm} = I_i \left[\cos(\alpha)\sin(\beta)\cos(\psi - \gamma) + \sin(\alpha)\cos(\beta)\right]$$

where I_i is the direct intensity of incident light (1000 W/m^2), α is the elevation angle of the sun, β is the PV tilt angle, γ is the sun azimuth angle, and ψ is the azimuth angle that the PV faces. The calculated data are presented in fig. S6, and the radiation from atmospheric scattering or ground reflection is not considered for simplifying. The amount of radiation reaching the WSOD exhibits a similar trend to the measured values, and, for the conditions of 45° and 60°, it is calculated to be zero according to the given assumptions. These data suggest that an adequate amount of power for device operation can be obtained during the whole daytime. This implies that there are no temporal constraints during daylight hours, and the solar cell can obtain a sufficient amount of power during outdoor activities.

EQE spectrum of dual junction solar cell, as seen in Fig. 2C, is capable of accommodating a wide range of wavelengths, allowing

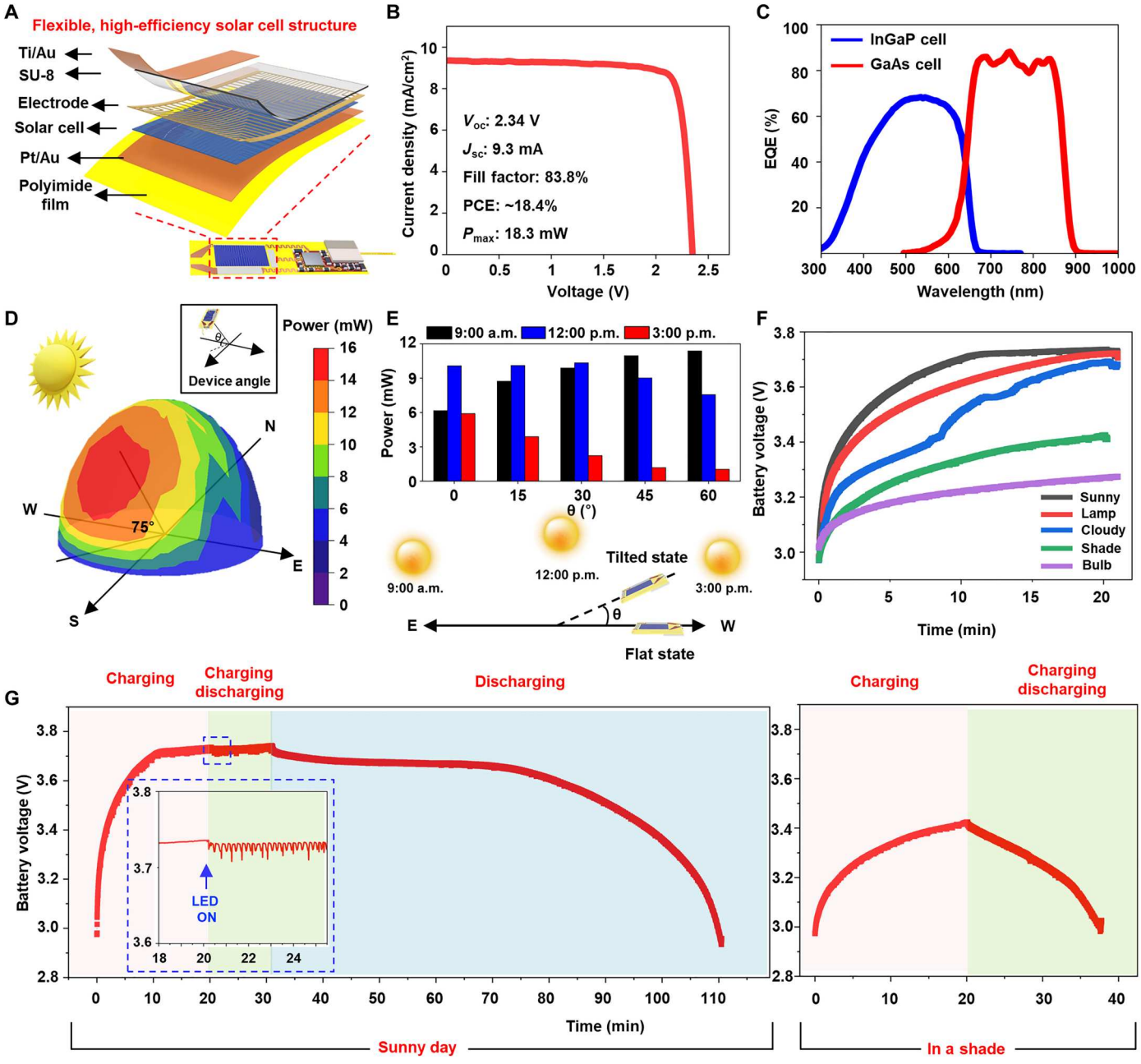

Fig. 2. Flexible solar cell characteristics and harvesting characteristics of WSOD in various atmosphere. (**A**) Exploded view schematic diagram of flexible, high-efficiency InGaP/GaAs tandem solar cell integrated with WSOD. (**B**) Current density (*J*)–voltage (*V*) for flexible solar cells and basic solar cell characteristics. (**C**) Corresponding external quantum efficiency (EQE) data for the dual-junction solar cells. (**D**) A hemispherical color mapping three-dimensional (3D) graph of the harvested energy according to the tilted degree from the sunlight power source at noon. Inset image for viewing angle of the device. N, north; E, east; W, west; S, south. (**E**) Harvested energy from WSOD at different times (9:00 a.m., 12:00 p.m., and 3:00 p.m.) with different tilted degrees (0°, 15°, 30°, 45°, and 60°). The bottom illustration shows the different sun locations along the time and the device tilted angle. (**F**) Wireless battery charging characteristics in various environments and light sources. (**G**) Monitoring of battery voltage levels in two different atmospheres (sunny day, in a shade) with different device operating statuses. Pink background, device charging without operating for 20 min. Green background, device charging during LED operating. Blue background, LED operating with blocked sunlight. The inset graph is an enlarged view when the μ-LED is turned on.

the cell to effectively absorb light in any situation using different conditions of light sources with different intensities and wavelengths. Figure 2F and fig. S7 present a graph depicting the charging time for various environments and light sources, ranging from 3.0 up to 3.7 V. Because sunlight has a broad wavelength spectrum with high intensity, the device charged in just 10 min under clear skies with 15-mW power generation. Charging with a lamp, placed 20 cm away from the device [fig. S8 for the two-dimensional (2D) plot of the harvested energy], also reached 3.7 V after approximately 20 min. On cloudy days, the charging graph fluctuated due to the influence of clouds on light exposure, but ultimately, the charging was completed in 20 min. Even in the case of the device placed in the shadow on a clear day, sufficient charging was achieved due to light reflection, allowing the solar cell to absorb light energy. However, in the case of a bulb light source, charging was minimal due to the low power and limited wavelength spectrum (table S2 for power generation of various light sources). Figure 2G displays the charging and discharging profile of the device on a clear day and under challenging outdoor conditions in a shaded environment. Starting from the battery's minimum allowable voltage of 3.0 V, the device reaches full charge in 10 min under clear-sky conditions. The overcharge protection function in the power management circuit prevents the voltage from exceeding a certain level even if it continues to charge for an additional 10 min (pink background, "charging" section). Subsequently, the device is charged while simultaneously turning on the μ-LED for 10 min (green background, "charging and discharging" section), with the enlarged graph view representing the situation when the μ-LED was turned on at 20 min (10% duty, 20 Hz). The sustained voltage level indicates that the power consumption during device operation is lower than the power provided during charging, and this suggests that the device can operate continuously as long as a light supply is available. In addition, the graph illustrates the possibility of device operation without an external power supply by blocking the supply of solar energy and only activating the μ-LED after 30 min from the initial charging (blue background, "discharging" section). Considering that it took 10 min to reach 3.7 V, the result demonstrates that the device can operate for nearly 80 min afterward, proving its effectiveness in enabling device usage with a ratio of eight times compared to the charging and discharging time. The right graph in Fig. 2G shows the charging and discharging graph in a shade. Despite only achieving a voltage of approximately 3.4 V after 20 min of charging in the shade, the device's ability to operate for nearly 20 min afterward suggests that relatively unrestricted activities can be performed in outdoor spaces. These results provide important insights for the development of sustainable and self-sufficient devices in the field of renewable energy and demonstrate the potential for future applications of this technology.

Mechanical, thermal, and optical properties of WSOD

For stable implantation and attachment of the device on the head, miniaturization of the device is necessary. To achieve this, the solar cell and other components including power management and wireless communication were separated into distinct circuit regions, allowing for a 180° folding process. The battery was positioned between the folded sections, as shown in Fig. 3A, which depicts the device conformally bent around a cylindrical tube with a radius of curvature of 1.5 mm. Mechanical folding induces large, local bending and stretching deformations depending on the interconnect structure. To ensure minimal impact on device performance, the bending structure for the integrated circuit is designed to exhibit an elastic response under such circumstances, as demonstrated through the finite element method (FEM). Figure 3B and figs. S9 and S10 show the FEM results for interconnect lines within the folding area, comparing straight and serpentine lines. In the case of straight interconnect lines, plastic deformation occurred globally across the line, with a maximum value of 1.09% that significantly exceeds the plastic yielding point of copper (~0.3%) (*41*). In contrast, the serpentine structure exhibited elastic deformation, with even the strain concentration zones showing a maximum strain value of 0.112%, resulting in stable mechanical deformation. The observed absence of plastic deformation in serpentine interconnects, as opposed to the occurrence in straight interconnects, confirms that there are no mechanical issues concerning the circuit operation of the device.

Optogenetic stimulation using μ-LED can result in a local temperature increase at the stimulation site due to light emission and heat dissipation. The temperature increase can cause brain tissue damage, hindering effective optogenetic stimulation and, in severe cases, leading to seizures (*3*). For medical devices, temperature changes must be within 1°C to meet safety standards [International Organization for Standardization (ISO) 14708-1:2014(E)]. Thus, enabling effective optogenetic stimulation with minimal temperature changes using μ-LED probes is crucial, and this can be achieved by adjusting the duty cycle, the ratio of on and off time for the μ-LEDs. On the basis of a suitable frequency of 20 Hz for optogenetics (*3*, *20*), we measured the temperature changes in the probe within the brain tissue, assumed to be at 36°C, over 3 min as a function of the duty cycle (Fig. 3C and fig. S11). At a 10% duty cycle, the maximum change was within 1°, satisfying the ISO standard, while higher duty cycles exhibited larger temperature changes. As the μ-LED is controlled by GPIO control through the Bluetooth system, the supplied voltage had minimal influence on temperature (fig. S12). Therefore, a 10% duty cycle at a 20-Hz frequency is adopted as the stimulation parameter to achieve the most minimal temperature change.

For optogenetic applications that elicit circling behavior, the LED's light power density must be within the range of 6 to 40 mW/mm^2 (*3*, *20*). Light power density is heavily influenced by the light power emitted from the μ-LED, which is known to be dependent on the driving current. Therefore, if the battery voltage is excessively high (>3.8 V), then μ-LED may emit blue light with high intensity (over 1 mW). To prevent this, the LED's optical power is intentionally adjusted through a connected resistor to achieve a density below 40 mW/mm^2. Figure 3D presents the graphs before and after power regulation through a resistor connection. When the supplied voltage is 3.8 V or lower following regulation, effective optogenetic stimulation can be achieved. Figure 3E shows the voltage and current across the μ-LED when the duty cycle is set to 10%, and regulation is performed on the basis of the obtained data with 20-Hz frequency performance after regulating. Figure 3F in the optical stimulation results reveals that, when using μ-LED to stimulate the M2 region of the mouse brain at a density of 40 mW/mm^2, the light intensity decreases by half at approximately 50 μm from the source and reaches 5 mW/mm^2 at a distance of 0.2 mm. On the basis of μ-LED power and threshold of cell activation, the effective stimulation resolution can be restricted to the range of several hundreds of micrometers (*42*).

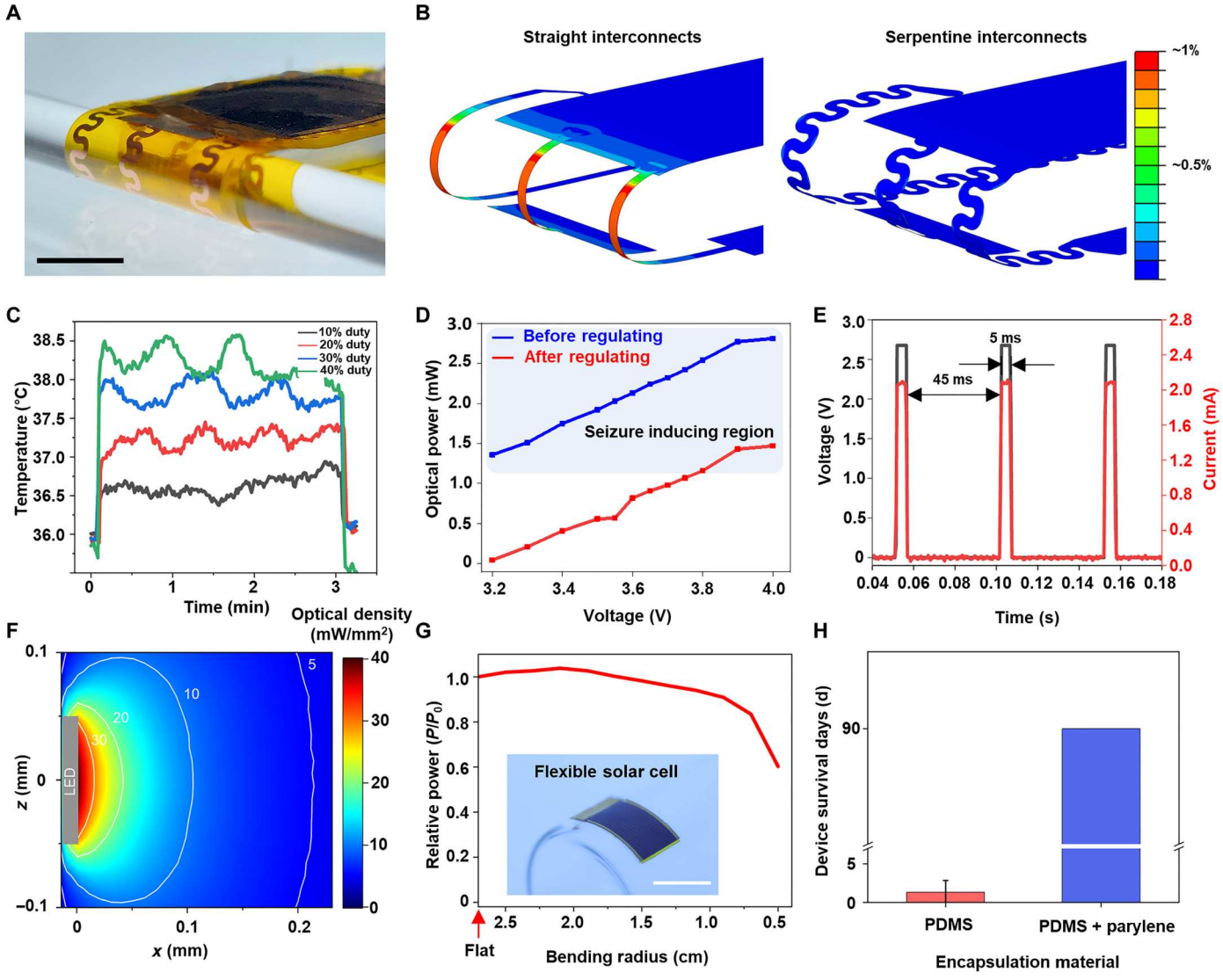

Fig. 3. Mechanical, optical, and thermal properties of WSOD. (**A**) Optical image of the folding area in miniaturized WSOD bending radius: 1.5 mm. Scale bar, 5 mm. (**B**) Strain distribution results of shell element FEM simulation with straight interconnects (left) and serpentine interconnects (right) near the folding area. The serpentine structure has less applied strain than the straight one. (**C**) Temperature changes of μ-LED operated at different duty cycles (5-, 10-, 15-, and 20-ms pulse width with 20-Hz frequency). To mimic the brain implantation, the base starting temperature is 36.0°C using a hot plate. (**D**) Optical power from the μ-LED at various battery voltages before (blue line) and after regulating (red line) by connecting a resistor for preventing excessive photostimulation (>1 mW). (**E**) Output voltage and current from μ-LED with 20-Hz frequency and duty cycle of 10% at 3.7-V battery level. (**F**) Estimated spread of light in the brain during μ-LED illumination with density of 40 mW/mm^2 at the LED surface. (**G**) The relative harvested power according to the various bending radius. The reference point is the harvested power in a flat state, and the light source (lamp) is located 20 cm above the device. Scale bar, 1 cm. (**H**) Device survival lifetime in PBS at room temperature when encapsulated with a monolayer of PDMS or a bilayer of parylene C and PDMS (n = 3).

After mounting WSOD on the head, obtaining durability is crucial because the skin also moves along with the subject's movements. Using flexible high-efficiency solar cells can make the device durable over movements and ensure that its energy-harvesting function remains largely unaffected under device bending. Figure 3G depicts the energy-harvesting ratio of the PV device as its transition from a flat state to various bending degrees. The harvested power gradually decreases as the bending radius reduces to 2 cm and then rapidly declines at 1 cm, eventually resulting in the loss of the solar cell's functionality due to effective area loss and physical damage caused by a mechanical strain. The maintenance of the solar cell's energy-harvesting capability up to a bending radius of 2 cm indicates that the device even with a slightly bent state can provide a stable power supply after being attached to the head. In addition, for ensuring proper photostimulation, a protective barrier against external disturbances such as biofluids, dust, and shock is necessary. Figure 3H demonstrates the device's durability within phosphate-buffered saline (PBS). When only using PDMS as the encapsulation layer, the device lost its functionality within 4 days. However, when using parylene C (~8 μm) and PDMS, the device demonstrated stable operation over 90 days in a biofluid environment, indicating high potential as a device for chronic in vivo

studies. As the encapsulation is one of the most important considerations in designing implantable bioelectronics, for a longer and safe use, there have been many encapsulation studies for the protection of both the subject and device. For example, additional deposition of inorganic materials along the parylene C and PDMS encapsulation can markedly improve the barrier properties against ion or water penetration (*43*–*46*).

Wireless optical stimulation with WSOD and monitoring of behavioral changes

To validate the functionality of WSOD for optogenetic stimulation, we implanted the probe into brain M2 of C57BL6 Thymus cell antigen 1–Channelrhodopsin 2–Yellow Fluorescent Protein (Thy1-ChR2-YFP) transgenic mice and assessed the change of locomotion behavior in response to 20 Hz, 10% duty cycle stimulation with 460-nm blue light (Fig. 4A). Previous research has established that stimulating M2 can result in circling behavior (*3*, *15*, *20*). After the device implantation, the stimulating probe was fixed with a small amount of dental cement to fix the probe and prevent any movement of the device during locomotion behavior (fig. S13 for implant process). Figure 4B displays an optical image of a mouse with an implanted WSOD on artificial turf, demonstrating the capability of wireless charging and stable device operation while the subject moves freely within a spacious environment.

After implantation of WSOD, animals are allowed to have a recovery period before the behavior experiment, and we monitored changes in locomotor activity induced by optical stimulation. To observe the circling behavior induced by photostimulation, a mouse was placed in a behavior test box (50 cm by 50 cm; Fig. 4C). The experiment lasted for a total of 15 min, which involved alternating between turning the μ-LED off and on (~35 mW/mm^2) for 3 min each. The first epoch was used to establish the baseline level of locomotor activity, and the third and fifth epochs were conducted in the absence of photostimulation. In contrast, the second and fourth epochs involved photoillumination to the target area for assessing the impact of photostimulation (Fig. 4D). During the stimulation epoch, we observed compulsive circling behaviors and increased moving velocity. In contrast, mice without stimulation moved randomly at lower velocities as expected from previous works (Fig. 4E). We quantitatively analyzed the changes in behaviors in terms of (i) the number of circling behaviors, (ii) total travel distance, and (iii) time spent in mobility on several mice. Photostimulation with our WSOD induced increases in the contralateral circling, and there was a significant difference in circling behavior between μ-LED on epoch and μ-LED off epoch (Fig. 4F and movie S2). When the μ-LED was turned off, the mice exhibited an average of 0.5 rotations/min; however, when the μ-LED was turned on, the average increased to over 4 rotations/min. In addition, this photostimulation in the M2 induced an increase in the total travel distance of the animals significantly (Fig. 4G). When the μ-LED was turned on, the animals traveled an average of over 20 m, whereas the animal traveled around 10 m when the μ-LED turned off. Furthermore, during the photostimulation, they showed a significant difference in mobility time between the off epoch and on epoch (Fig. 4H). During the μ-LED was turned off, they spent less than 70% of their time in mobility while during the stimulation epoch, the mice spent much more time in mobility, over 80%. Through these results, we successfully demonstrated that the fabricated WSOD showed reliable stimulation on the M2 region of the behaving mouse.

To demonstrate the chronic, repetitive, and stable photostimulation of the WSOD, the behavioral experiment was conducted once a week over 1 month on the same individual mouse. As shown in Fig. 4I, we performed 4 weeks of 15-min photostimulation sessions, and the behaviors of mice were analyzed in terms of circling, total distance, and time spent in mobility as we did in Fig. 4 (F to H). Compared to the off epoch of the stimulation session, each photostimulation that was performed once a week induced the circling behavior more than three turns in a minute, traveled more than 15 m, and spent time more than 90% in mobility. These consistent results, observed over the course of a month, show similar trends of behavior changes induced by photostimulation across multiple individuals as shown in Fig. 4 (I to K) (fig. S14). The repetitive results showed that the chronically implanted probe could stimulate the M2 region for 1 month stably. Namely, while the experiment was conducted over 4 weeks, continuous optical stimulation could be provided throughout the animal′s lifetime without constraining its behavior with this device.

The benefits and demonstration of potential applications using WSOD

The most beneficial advantage of the WSOD is its ability to charge without any external instruments, allowing users to operate in a completely unrestricted environment without hindering their freely behaving subjects. This can be achieved due to the device′s minimal power consumption relative to harvested power, which allows it to obtain and store sufficient energy for operation in a short period. To demonstrate this, we measured the battery voltage corresponding to automatic charging and device operation (Fig. 5A). The WSOD was placed by a window with relatively weak sunlight (due to the optical property of the glass window) for 7 days. Throughout this period, the device charged automatically according to the amount of sunlight naturally entering the room each day. After sunset, the device′s LED was activated through BLE, starting daily at 8:00 p.m. On the first day, the device operated for 30 min, for 1 hour on days 1 to 2, for 2 hours on days 3 to 5, and for over 2 hours and 30 min on days 6 to 7. Because battery voltage is not an absolute indicator of the state of charge and the slow charging process allows the battery to store more charge, the device was capable of operating for up to 2 hours and 30 min (*47*, *48*). The blue enlarged graph in Fig. 5A displays the voltage profile over a 24-hour period, starting at 12:00 a.m. on day 4 and ending at 12:00 a.m. the following day. Approximately after 6:00 a.m., as the sun begins to rise, the device initiates the charging process, enabling continuous Bluetooth connectivity until the evening while maintaining its operational state. During a 2-hour operation period starting at 8:00 p.m., the battery voltage gradually decreases. Once the operation is temporarily halted, the battery voltage undergoes a slight recovery due to the battery voltage restoration while keeping continuous Bluetooth connectivity (*49*). This demonstrates that the device can obtain sufficient power and operate chronically without any external charging equipment. Figure 5B illustrates the potential operation and characteristics of the device when applied to humans, based on a daily routine. As the sun begins to rise in the early morning, the device gradually charges. If the device has not been used continuously for over 2 hours and 30 min, then the Bluetooth signal remains detectable by mobile phones. During the day,

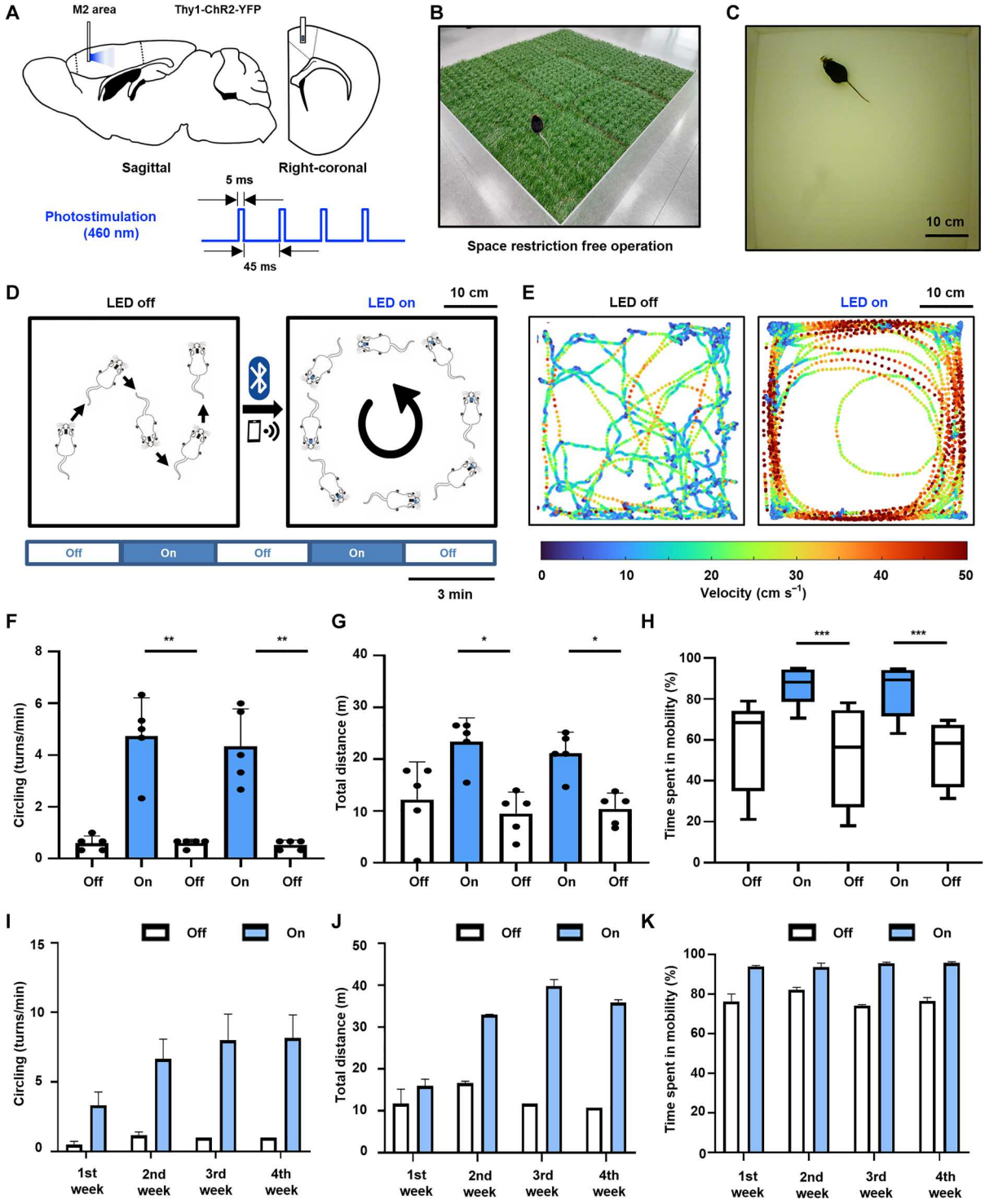

Fig. 4. Optogenetic stimulation of brain M2 area for locomotion behavior. (**A**) Schematic diagram of μ-LED probe insertion into mouse brain M2 (sagittal and right-coronal) and 460-nm photoillumination. (**B**) An optical image of a mouse with an implanted WSOD on artificial turf without any external equipment. (**C**) Photograph of a transgenic mouse in a behavior test box. (**D**) Overview of in vivo experiment of eliciting circling behavior by stimulating with 3-min interval. (**E**) Comparison in the velocity tracking map when the μ-LED is turned on and off. (**F** to **H**) Behavior analysis during on and off epoch with 3-min intervals. (F) Circling numbers. (G) Total distance. (H) Time spent in mobility. (**I** to **K**) Repetitive behavior analysis of a single mouse conducted once a week for a month. (I) Circling numbers. (J) Total distance. (K) Time spent in mobility. *$P < 0.05$, **$P < 0.01$, ***$P < 0.001$.

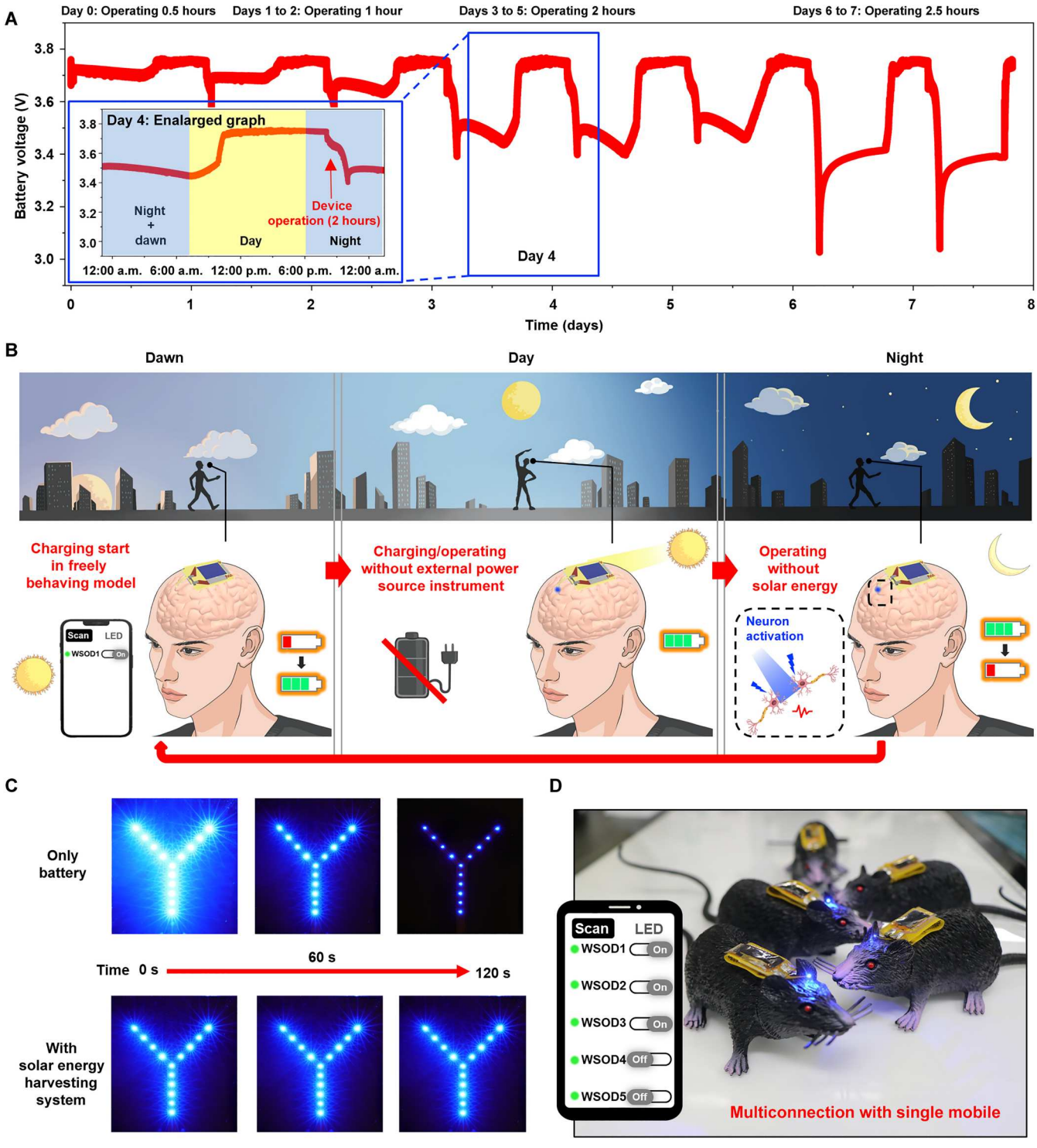

Fig. 5. Conceptual demonstration of WSOD for chronic use and multiconnection. (**A**) Battery voltage level monitoring of WSOD according to the time of day for a week. Autocharging starts with sunrise and fully charged before noon, demonstrating chronic use of WSOD. Blue μ-LED is turned one at 8:00 p.m. every night with different operating times (day 0, 0.5 hours; days 1 to 2, 1 hour; days 3 to 5, 2 hours; and days 6 to 7, 2.5 hours). The blue box shows the enlarged graph of day 5, which shows the change of voltage level according to the time. (**B**) Conceptual illustration showing the cycles of wireless recharging and operating during outdoor activity for human brain application. After sunset charging starts, the device is fully charged without an external power source and spatial constraints. Energy storage enables humans to operate WSOD even at night. (**C**) The brightness of parallelly connected blue LEDs with only battery/with solar energy-harvesting system. Using only a battery results in low–power efficiency consumption. The solar energy-harvesting system operates the device with high efficiency by regulating power. (**D**) Multiconnecting operation with several subjects with a single mobile.

the battery can be sufficiently charged, and, with the overvoltage protection feature, it remains safe as users carry on with their daily activities. A mere 10 min of outdoor activity is enough to charge the device without any external equipment or chargers. Although natural charging is not possible at night, the device's internal energy storage enables it to operate during the night. If necessary, indoor light sources can be used for an additional charge. In this manner, the cycle continues indefinitely, enabling the device to serve as a tool for brain disorder treatment in daily life, regardless of time and location.

WSOD offers several advantages as it not only overcomes spatiotemporal limits but also facilitates efficient management and regulation of power consumption. Figure 5C compares power regulation when only a battery is present and when a solar energy harvester is integrated. After implementing a Y-shaped configuration by connecting 12 LEDs in parallel and operating them with dc power from a battery only, the initial brightness is the strongest but rapidly decreases within 2 min due to rapid discharge. However, the basic form of solar energy harvester with a constant light source enables precise power regulation, and the brightness is maintained consistently over time. Figure 5D demonstrates the advantages of using a Bluetooth system for optogenetics. A single mobile phone can manage multiple connections through a customized mobile application that enables simultaneous in vivo experiments on multiple subjects (fig. S15 and movie S3). In addition, because programmable tools are supported, further development could allow for different frequency-LED control for each subject, providing various types of stimulation. The multiconnection and programmable selective control features are expected to have a highly positive impact on neuroscience research by allowing the observation of diverse responses to different stimuli in the medical context, with the ability to optogenetically control individual subjects.

DISCUSSION

We have introduced a wirelessly rechargeable and controllable optogenetic device based on solar energy harvesting, which allows wireless charging without spatial constraints, unlike traditional device operation or charging methods. The ability to recharge naturally during routine daily activities without the need for large, expensive equipment such as RF generators or amplifiers is the most powerful advantage that enables the ultimate goal of completely freely behaving wireless optogenetic devices. The capability to control devices individually through a mobile phone application without the need for additional external equipment allows for the administration of different stimuli to each subject and the observation of their reactions. By providing an accessible and versatile experimental environment for control anytime and anywhere, this technology not only contributes to the elucidation of brain circuits but also offers a substantial potential for the treatment of neurological disorders.

Despite the numerous advantages offered by the device, there are still chances for further development. To advance toward an ultraminiaturized device, the current small-sized device should be significantly reduced in dimension by using even smaller power management circuit components (e.g., 0201 chip packaging) and using ultrathin polymer batteries to reduce the overall thickness of the device. Furthermore, the Bluetooth GPIO pins can accommodate multiple types of stimulators or recording electrodes. This would enable high-density stimulation and simultaneous stimulation of multiple areas, providing more advanced technology. The solar-powered optogenetics device, equipped with the abovementioned features, enables true freely moving experiments, as opposed to the tethering or restricted cage activities that result in half freely moving conditions. In addition, also by integrating perovskite solar cell rather than III-V solar cell, WSOD can more efficiently charge in indoor ambient environment. In the near future, this technology could be used to obtain optogenetic data from primate models in their natural states. Furthermore, if applied to humans, then the device eliminates the need to remain stationary or connected to wires for charging, ensuring that individuals can engage in their natural activities without any disruption. The technology holds potential for significant contributions to the treatment of neurological disorders, such as Parkinson's disease, and other related conditions. The presented device in this research paves the way for innovative avenues in in vivo experimentation while considerably augmenting user utility, rendering it an exceptionally valuable and multifaceted technology.

MATERIALS AND METHODS

Fabrication of high-efficiency InGaP/GaAs tandem flexible solar cells

PI film (Kapton, DuPont, ~13 μm) was used as a flexible substrate. PDMS (10 μm) was spin-coated on Si, and the PI film was laminated with the Si. The solar cell wafer and the PI film were cleaned using acetone, methanol, and deionized (DI) water, followed by deposition of Pt/Au (10/60 nm) on the solar cell wafer and PI film, respectively, using an electron-beam (e-beam) evaporator (Korea Vacuum Tech, Korea). The solar cell wafer and the PI film were bonded using a metal wafer bonding technique (*29*, *50*, *51*). For metal bonding, the surfaces of the solar cell and PI film are activated by Ar plasma and then bonded using a wafer bonder under conditions of 200°C and 40 kgf/cm^2. GaAs-based materials were etched using an H_3PO_4:H_2O_2:DI water (1:1:5) solution until the GaAs contact layer is exposed, while InGaP-based materials were etched using an H_3PO_4:HCl (3:1) solution. After etching, negative photoresist (AZ 2035, MicroChemicals) was used for photolithography to form top electrode and grid line patterns, which were then deposited using an e-beam evaporator with Pd, Ge, and Au (20/40/300 nm). Liftoff was performed using acetone to form the top electrode and grid lines. Dry etching using Cl-based gas was performed in an Inductively Coupled Plasma-Reactive Ion Etching (ICP-RIE) chamber for mesa isolation of the fabricated device. Next, Au contact pads were formed to integrate the device with a Bluetooth system. Negative photoresist SU-8 was spin-coated at 2000 rpm for 30 s onto the fabricated device, followed by via formation and hard baking of the SU-8 at 160°C for 30 min. Using AZ 2035, the Au contact pads patterns were formed, and Au (500 nm) was deposited using sputtering (SME-200E, ULVAC, Japan) for the Au contact pads.

Fabrication of WSOD

The whole fabrication process is described in fig. S16. Flexible device fabrication begins with spin-coating degassed 10:1 PDMS (base:curing agent) on a clean glass slide. After baking on a hot plate at 80°C for 24 hours, 25-μm PI film (DuPont) is laminated onto the glass. The bottom copper layer is deposited through a

thermal evaporator, and conducting traces are defined by standard photolithography with a photoresistor (AZ5214-E, AZ Electronic Materials) and developer (AZ 300 MIF Developer, Merck & Co. Inc.). In addition, second PI [poly(pyromellitic dianhydride-*co*-4,4′-oxydianiline), amic acid solution from Merck Sigma-Aldrich solutions], which serves as an insulating layer is formed by spin casting at 3000 rpm for 30 s and cured at 210°C for 2 hours. The second PI layer is etched for interconnection via in the circuit through standard photolithography (AZ4620, AZ Electronic Materials) and reactive ion etching. To finish the circuit interconnects, the top copper layer is patterned as the bottom layer after deposition. Circuit chips are soldered onto the exposed pad by using low-temperature solder paste (SMDLTLFP, Chip Quik). The device is cut following the outline with a commercial razor blade and subsequently detached from the glass substrate after fixing the chip location with ultraviolet curable polymer. The battery leg and the device center region are folded to achieve miniaturization. Glue is applied to both sides of the battery to maintain the folded state. Following the coating of the device with parylene C via chemical vapor deposition, the outer shell is encapsulated using PDMS.

Electronic device components

The solar energy-harvesting module is equipped with an MPP tracking feature, which effectively converts the energy harnessed from solar cells into an appropriate form for battery charging and device operation. For controlling the harvesting process, a microcontroller (Bq25570, Texas Instrument, 3.5 mm by 3.5 mm) served as a power boost charger and buck converter for energy harvester-powered applications. BLE SoC (MBN52832, Murarta, 7.4 mm by 7.0 mm) enables controlling photostimulation through a mobile application, which is programmed by Segger Embedded Studio (SES). The commercial mobile application is nRF Blinky from Nordic, and the custom-built smartphone application was developed using the Kotlin programming language in the Android Studio development environment. A rechargeable polymer lithium-ion battery (GEB020815, GE Battery Co. Limited) supplies stable dc voltage to BLE SoC, and μ-LED (C460SR1321, Cree Led, 210 μm by 130 μm, *I-V* curve for fig. S17) for stimulation is limited by a resistor for preventing excessive stimulation. For circuit operation, most auxiliary capacitors and inductors are in 0402 packaging size, and 22- and 10-μH inductors are in 0603 packaging size.

Mechanical analysis of folding area with serpentine and straight interconnects

The commercial software ABAQUS/CAE 2022 was used to analyze the serpentine and straight interconnects with corresponding structure layouts and material properties. For the WSOD device, all parts, including PI, PDMS, and copper layers, were modeled with composite shell elements (S4R). The elastic modulus and Poisson′s ratio values are 90 GPa and 0.34 for copper, 2.5 GPa and 0.34 for PI, and 10 Mpa and 0.49 for PDMS, respectively. In addition, the plastic deformation of copper was modeled by considering its strain-hardening property (*52*), and the elastic-plastic homogeneous isotropic model was used for PI (*53*). After fixing the middle in the WSOD folding range, the rotational displacement boundary conditions were applied to the far end of the device to simulate the folding process.

Optical analysis of illumination in mouse brain

To verify the light distribution in the mouse brain, the 3D ray-tracing simulations based on the Monte Carlo method were conducted using commercial software (OpticStudio 16.0, ZEMAX Inc.). In the simulation, a monochromatic (465-nm) rectangular-shaped radial source (190 μm by 110 μm in the x and y directions) with an intensity of 1 mW was used as a light source. The angular power of the light source in the simulation appears in fig. S18 (*54*). The optical constants for the mouse brain were applied to the background material (table S3). The volume detector (4 mm by 4 mm by 4 mm) with the pixels of 200 × 200 × 200 in the x, y, and z directions was used to record the light distribution at the center position of the y axis. Rays (5×10^7) were used to obtain reliable calculation results.

Measurement of temperature and optical power during μ-LED operation

To verify the thermal safety depending on the ratio of μ-LED on and off, the temperature was measured for each duty cycle using a digital thermometer (TX10, Yokogawa). The probe duty cycle was programmed each time using SES, and the probe was placed on a hot plate (HSD150-03P) to maintain a temperature of 36.0°C to simulate the brain environment. To prevent overstimulation, the optical intensity was measured using an optical powermeter (PM100, Thorlabs) at the 460-nm wavelength point. In addition, a digital multimeter (DAQ6510, Keithley) enables voltage and current measurements on the LED during the optical measurement.

Stereotaxic surgery

To perform optical stimulation of the secondary motor cortex, adult male transgenic mice (C57BL6 Thy1-ChR2-YFP; aged 8 weeks, weighing between 25 and 30 g) were subjected to WSOD. The mice were initially anesthetized with 3% isoflurane to induce unconsciousness and were maintained under 1 to 1.5% isoflurane during surgeries. An isoflurane vaporizer (SurgiVet Classic T3 vaporizer, Smiths Medical Inc., Minneapolis, MN, USA) was used to administer the anesthesia. Once the mouse was anesthetized, it was positioned on a stereotaxic instrument (David Kopf Instruments, USA), and the hair and scalp were removed. We targeted the secondary motor cortex (M2) at coordinates—anterior-posterior of 1.2 mm, medial-lateral of 0.6 mm, and dorsal-ventral of −1.25 mm—from bregma and inserted the device slowly into the M2 area after drilling the target site based on the atlas of Paxinos and Franklin (*55*). The inserted WSOD was fixed on the skull with four screws and a small amount of dental cement (Vertex Self Curing, Vertex Dental, The Netherlands). After fixation of the probe part of the WSOD, the whole device is folded on the head, and a small amount of dental cement is applied under the device to firmly fix on the mouse head. Following the surgical procedure, each mouse was housed separately to allow for 7 days of adequate recovery time and to prevent any potential behavioral disruptions from other mice.

Behavioral analysis

To induce contralateral circling of the behaving mouse, we turned on the μ-LED of the WSOD with the application of a smartphone through Bluetooth communication. Animal tracking software products, specifically idTracker (*56*), were used for behavior analysis. The trajectory plots of the behaving mouse were expressed using MATLAB. In the case of behavior analysis, the data obtained were subjected to a two-way analysis of variance (ANOVA), with the

individual epochs as the repeated measures and two epochs (LED on versus off) as the independent variables for analysis. All statistical analysis was performed using Prism (GraphPad software).

Supplementary Materials

This PDF file includes:
Figs. S1 to S18
Tables S1 to S3
Legends for movies S1 to S3

Other Supplementary Material for this manuscript includes the following:
Movies S1 to S3

REFERENCES AND NOTES

1. K. Deisseroth, Optogenetics. *Nat. Methods* **8**, 26–29 (2011).
2. O. Yizhar, L. E. Fenno, T. J. Davidson, M. Mogri, K. Deisseroth, Optogenetics in neural systems. *Neuron* **71**, 9–34 (2011).
3. L. A. V. Magno, H. Tenza-Ferrer, M. Collodetti, M. F. G. Aguiar, A. P. C. Rodrigues, R. S. da Silva, J. d. P. Silva, N. F. Nicolau, D. V. F. Rosa, A. Birbrair, D. M. Miranda, M. A. Romano-Silva, Optogenetic stimulation of the M2 cortex reverts motor dysfunction in a mouse model of Parkinson's disease. *J. Neurosci.* **39**, 3234–3248 (2019).
4. M. C. Walker, D. M. Kullmann, Optogenetic and chemogenetic therapies for epilepsy. *Neuropharmacology* **168**, 107751 (2020).
5. K. T. Vann, Z.-G. Xiong, Optogenetics for neurodegenerative diseases. *Int. J. Physiol. Pathophysiol. Pharmacol.* **8**, 1–8 (2016).
6. R. C. Wykes, D. M. Kullmann, I. Pavlov, V. Magloire, Optogenetic approaches to treat epilepsy. *J. Neurosci. Methods* **260**, 215–220 (2016).
7. D. R. Sparta, A. M. Stamatakis, J. L. Phillips, N. Hovelsø, R. van Zessen, G. D. Stuber, Construction of implantable optical fibers for long-term optogenetic manipulation of neural circuits. *Nat. Protoc.* **7**, 12–23 (2012).
8. T. Moser, Optogenetic stimulation of the auditory pathway for research and future prosthetics. *Curr. Open. Neurobiol.* **34**, 29–36 (2015).
9. M. Hashimoto, A. Hata, T. Miyata, H. Hirase, Programmable wireless light-emitting diode stimulator for chronic stimulation of optogenetic molecules in freely moving mice. *Neurophotonics* **1**, 011002 (2014).
10. R. Qazi, A. M. Gomez, D. C. Castro, Z. Zou, J. Y. Sim, Y. Xiong, J. Abdo, C. Y. Kim, A. Anderson, F. Lohner, S. H. Byun, B. Chul Lee, K. I. Jang, J. Xiao, M. R. Bruchas, J. W. Jeong, Wireless optofluidic brain probes for chronic neuropharmacology and photostimulation. *Nat. Biomed. Eng.* **3**, 655–669 (2019).
11. J. G. McCall, R. Qazi, G. Shin, S. Li, M. H. Ikram, K. I. Jang, Y. Liu, R. al-Hasani, M. R. Bruchas, J. W. Jeong, J. A. Rogers, Preparation and implementation of optofluidic neural probes for in vivo wireless pharmacology and optogenetics. *Nat. Protoc.* **12**, 219–237 (2017).
12. G. Gagnon-Turcotte, E. Maghsoudloo, Y. Messaddeq, Y. De Koninck, B. Gosselin, in *2017 15th IEEE International New Circuits and Systems Conference (NEWCAS)*, Strasbourg, France, 25 to 28 June 2017 (IEEE, 2017), pp. 193–196.
13. C. T. Wentz, J. G. Bernstein, P. Monahan, A. Guerra, A. Rodriguez, E. S. Boyden, A wirelessly powered and controlled device for optical neural control of freely-behaving animals. *J. Neural Eng.* **8**, 046021 (2011).
14. Y. Iwai, S. Honda, H. Ozeki, M. Hashimoto, H. Hirase, A simple head-mountable LED device for chronic stimulation of optogenetic molecules in freely moving mice. *Neurosci. Res.* **70**, 124–127 (2011).
15. J. Ausra, M. Wu, X. Zhang, A. Vázquez-Guardado, P. Skelton, R. Peralta, R. Avila, T. Murickan, C. R. Haney, Y. Huang, J. A. Rogers, Y. Kozorovitskiy, P. Gutruf, Wireless, battery-free, subdermally implantable platforms for transcranial and long-range optogenetics in freely moving animals. *Proc. Natl. Acad. Sci. U.S.A.* **118**, e2025775118 (2021).
16. K. N. Noh, S. I. Park, R. Qazi, Z. Zou, A. D. Mickle, J. G. Grajales-Reyes, K. I. Jang, R. W. Gereau IV, J. Xiao, J. A. Rogers, J. W. Jeong, Miniaturized, battery-free optofluidic systems with potential for wireless pharmacology and optogenetics. *Small* **14**, 1702479 (2018).
17. Y. Zhang, A. D. Mickle, P. Gutruf, L. A. McIlvried, H. Guo, Y. Wu, J. P. Golden, Y. Xue, J. G. Grajales-Reyes, X. Wang, S. Krishnan, Y. Xie, D. Peng, C. J. Su, F. Zhang, J. T. Reeder, S. K. Vogt, Y. Huang, J. A. Rogers, R. W. Gereau IV, Battery-free, fully implantable optofluidic cuff system for wireless optogenetic and pharmacological neuromodulation of peripheral nerves. *Sci. Adv.* **5**, eaaw5296 (2019).
18. P. Gutruf, R. T. Yin, K. B. Lee, J. Ausra, J. A. Brennan, Y. Qiao, Z. Xie, R. Peralta, O. Talarico, A. Murillo, S. W. Chen, J. P. Leshock, C. R. Haney, E. A. Waters, C. Zhang, H. Luan, Y. Huang, G. Trachiotis, I. R. Efimov, J. A. Rogers, Wireless, battery-free, fully implantable multimodal and multisite pacemakers for applications in small animal models. *Nat. Commun.* **10**, 5742 (2019).
19. A. D. Mickle, S. M. Won, K. N. Noh, J. Yoon, K. W. Meacham, Y. Xue, L. A. McIlvried, B. A. Copits, V. K. Samineni, K. E. Crawford, D. H. Kim, P. Srivastava, B. H. Kim, S. Min, Y. Shiuan, Y. Yun, M. A. Payne, J. Zhang, H. Jang, Y. Li, H. H. Lai, Y. Huang, S. I. Park, R. W. Gereau IV, J. A. Rogers, A wireless closed-loop system for optogenetic peripheral neuromodulation. *Nature* **565**, 361–365 (2019).
20. K. L. Montgomery, A. J. Yeh, J. S. Ho, V. Tsao, S. Mohan Iyer, L. Grosenick, E. A. Ferenczi, Y. Tanabe, K. Deisseroth, S. L. Delp, A. S. Y. Poon, Wirelessly powered, fully internal optogenetics for brain, spinal and peripheral circuits in mice. *Nat. Methods* **12**, 969–974 (2015).
21. S. I. Park, G. Shin, J. McCall, R. al-Hasani, A. Norris, L. Xia, D. S. Brenner, K. N. Noh, S. Y. Bang, D. L. Bhatti, K. I. Jang, S. K. Kang, A. D. Mickle, G. Dussor, T. J. Price, R. W. Gereau 4th, M. R. Bruchas, J. A. Rogers, Stretchable multichannel antennas in soft wireless optoelectronic implants for optogenetics. *Proc. Natl. Acad. Sci. U.S.A.* **113**, E8169–E8177 (2016).
22. Y. Yang, M. Wu, A. Vázquez-Guardado, A. J. Wegener, J. G. Grajales-Reyes, Y. Deng, T. Wang, R. Avila, J. A. Moreno, S. Minkowicz, V. Dumrongprechachan, J. Lee, S. Zhang, A. A. Legaria, Y. Ma, S. Mehta, D. Franklin, L. Hartman, W. Bai, M. Han, H. Zhao, W. Lu, Y. Yu, X. Sheng, A. Banks, X. Yu, Z. R. Donaldson, R. W. Gereau IV, C. H. Good, Z. Xie, Y. Huang, Y. Kozorovitskiy, J. A. Rogers, Wireless multilateral devices for optogenetic studies of individual and social behaviors. *Nat. Neurosci.* **24**, 1035–1045 (2021).
23. H. Zhang, P. Gutruf, K. Meacham, M. C. Montana, X. Zhao, A. M. Chiarelli, A. Vázquez-Guardado, A. Norris, L. Lu, Q. Guo, C. Xu, Y. Wu, H. Zhao, X. Ning, W. Bai, I. Kandela, C. R. Haney, D. Chanda, R. W. Gereau IV, J. A. Rogers, Wireless, battery-free optoelectronic systems as subdermal implants for local tissue oximetry. *Sci. Adv.* **5**, eaaw0873 (2019).
24. S. I. Park, G. Shin, A. Banks, J. G. McCall, E. R. Siuda, M. J. Schmidt, H. U. Chung, K. N. Noh, J. G. H. Mun, J. Rhodes, M. R. Bruchas, J. A. Rogers, Ultraminiaturized photovoltaic and radio frequency powered optoelectronic systems for wireless optogenetics. *J. Neural Eng.* **12**, 056002 (2015).
25. J. Jeong, J. Jung, D. Jung, J. Kim, H. Ju, T. Kim, J. Lee, An implantable optogenetic stimulator wirelessly powered by flexible photovoltaics with near-infrared (NIR) light. *Biosens. Bioelectron.* **180**, 113139 (2021).
26. S. Bhattacharya, S. John, Beyond 30% conversion efficiency in silicon solar cells: A numerical demonstration. *Sci. Rep.* **9**, 12482 (2019).
27. Y. Firdaus, V. M. Le Corre, J. I. Khan, Z. Kan, F. Laquai, P. M. Beaujuge, T. D. Anthopoulos, Key parameters requirements for non-fullerene-based organic solar cells with power conversion efficiency >20. *Adv. Sci.* **6**, 1802028 (2019).
28. S. M. Menke, N. A. Ran, G. C. Bazan, R. H. Friend, Understanding energy loss in organic solar cells: Toward a new efficiency regime. *Joule* **2**, 25–35 (2018).
29. T. S. Kim, H. J. Kim, D. M. Geum, J. H. Han, I. S. Kim, N. Hong, G. H. Ryu, J. H. Kang, W. J. Choi, K. J. Yu, Ultra-lightweight, flexible InGaP/GaAs tandem solar cells with a dual-function encapsulation layer. *ACS Appl. Mater. Interfaces* **13**, 13248–13253 (2021).
30. H. Hong, T. Huang, W. Uen, Y.-Y. Chen, Damp-heat induced performance degradation for InGaP/GaAs/Ge triple-junction solar cell. *J. Nanomater.* **2014**, 2 (2014).
31. S. Van Riesen, A. W. Bett, Degradation study of III–V solar cells for concentrator applications. *Prog. Photovolt. Res. Appl.* **13**, 369–380 (2005).
32. C. Y. Kim, M. J. Ku, R. Qazi, H. J. Nam, J. W. Park, K. S. Nam, S. Oh, I. Kang, J. H. Jang, W. Y. Kim, J. H. Kim, J. W. Jeong, Soft subdermal implant capable of wireless battery charging and programmable controls for applications in optogenetics. *Nat. Commun.* **12**, 535 (2021).
33. J. Shao, S. Xue, G. Yu, Y. Yu, X. Yang, Y. Bai, S. Zhu, L. Yang, J. Yin, Y. Wang, S. Liao, S. Guo, M. Xie, M. Fussenegger, H. Ye, Smartphone-controlled optogenetically engineered cells enable semiautomatic glucose homeostasis in diabetic mice. *Sci. Transl. Med.* **9**, eaal2298 (2017).
34. T.-i. Kim, J. G. M. Call, Y. H. Jung, X. Huang, E. R. Siuda, Y. Li, J. Song, Y. M. Song, H. A. Pao, R.-H. Kim, C. Lu, S. D. Lee, I.-S. Song, G. Shin, R. Al-Hasani, S. Kim, M. P. Tan, Y. Huang, F. G. Omenetto, J. A. Rogers, M. R. Bruchas, Injectable, cellular-scale optoelectronics with applications for wireless optogenetics. *Science* **340**, 211–216 (2013).
35. G. Shin, A. M. Gomez, R. al-Hasani, Y. R. Jeong, J. Kim, Z. Xie, A. Banks, S. M. Lee, S. Y. Han, C. J. Yoo, J. L. Lee, S. H. Lee, J. Kurniawan, J. Tureb, Z. Guo, J. Yoon, S. I. Park, S. Y. Bang, Y. Nam, M. C. Walicki, V. K. Samineni, A. D. Mickle, K. Lee, S. Y. Heo, J. G. McCall, T. Pan, L. Wang, X. Feng, T. I. Kim, J. K. Kim, Y. Li, Y. Huang, R. W. Gereau IV, J. S. Ha, M. R. Bruchas, J. A. Rogers, Flexible near-field wireless optoelectronics as subdermal implants for broad applications in optogenetics. *Neuron* **93**, 509–521.e3 (2017).
36. Y. Zhang, D. C. Castro, Y. Han, Y. Wu, H. Guo, Z. Weng, Y. Xue, J. Ausra, X. Wang, R. Li, G. Wu, A. Vázquez-Guardado, Y. Xie, Z. Xie, D. Ostojich, D. Peng, R. Sun, B. Wang, Y. Yu, J. P. Leshock, S. Qu, C. J. Su, W. Shen, T. Hang, A. Banks, Y. Huang, J. Radulovic, P. Gutruf, M. R. Bruchas, J. A. Rogers, Battery-free, lightweight, injectable microsystem for in vivo wireless pharmacology and optogenetics. *Proc. Natl. Acad. Sci. U.S.A.* **116**, 21427–21437 (2019).
37. A. Salim, S. Lim, Recent advances in noninvasive flexible and wearable wireless biosensors. *Biosens. Bioelectron.* **141**, 111422 (2019).

38. L. Wen, L. Yueqiang, C. Jianjun, C. Yanling, W. Xiaodong, Y. Fuhua, Optimization of grid design for solar cells. *J. Semicond.* **31**, 014006 (2010).
39. J. van Deelen, L. Klerk, M. Barink, Optimized grid design for thin film solar panels. *Solar Energy.* **107**, 135–144 (2014).
40. C. C. Ospina-Metaute, E. Betancur, L. F. Medina-Garzón, J. I. Marulanda-Bernal, A. Velásquez-López, in *Applied Computer Sciences in Engineering: 7th Workshop on Engineering Applications, WEA 2020*, Bogota, Colombia, 7 to 9, October 2020 (Springer, 2020), pp. 453–464.
41. J. W. Lee, R. Xu, S. Lee, K. I. Jang, Y. Yang, A. Banks, K. J. Yu, J. Kim, S. Xu, S. Ma, S. W. Jang, P. Won, Y. Li, B. H. Kim, J. Y. Choe, S. Huh, Y. H. Kwon, Y. Huang, U. Paik, J. A. Rogers, Soft, thin skin-mounted power management systems and their use in wireless thermography. *Proc. Natl. Acad. Sci. U.S.A.* **113**, 6131–6136 (2016).
42. F. Wu, E. Stark, P. C. Ku, K. D. Wise, G. Buzsáki, E. Yoon, Monolithically integrated μLEDs on silicon neural probes for high-resolution optogenetic studies in behaving animals. *Neuron* **88**, 1136–1148 (2015).
43. E. Song, R. Li, X. Jin, H. du, Y. Huang, J. Zhang, Y. Xia, H. Fang, Y. K. Lee, K. J. Yu, J. K. Chang, Y. Mei, M. A. Alam, Y. Huang, J. A. Rogers, Ultrathin trilayer assemblies as long-lived barriers against water and ion penetration in flexible bioelectronic systems. *ACS Nano* **12**, 10317–10326 (2018).
44. H. Fang, K. J. Yu, C. Gloschat, Z. Yang, E. Song, C. H. Chiang, J. Zhao, S. M. Won, S. Xu, M. Trumpis, Y. Zhong, S. W. Han, Y. Xue, D. Xu, S. W. Choi, G. Cauwenberghs, M. Kay, Y. Huang, J. Viventi, I. R. Efimov, J. A. Rogers, Capacitively coupled arrays of multiplexed flexible silicon transistors for long-term cardiac electrophysiology. *Nat. Biomed. Eng.* **1**, 0038 (2017).
45. H. Fang, J. Zhao, K. J. Yu, E. Song, A. B. Farimani, C. H. Chiang, X. Jin, Y. Xue, D. Xu, W. du, K. J. Seo, Y. Zhong, Z. Yang, S. M. Won, G. Fang, S. W. Choi, S. Chaudhuri, Y. Huang, M. A. Alam, J. Viventi, N. R. Aluru, J. A. Rogers, Ultrathin, transferred layers of thermally grown silicon dioxide as biofluid barriers for biointegrated flexible electronic systems. *Proc. Natl. Acad. Sci. U.S.A.* **113**, 11682–11687 (2016).
46. H.-P. Phan, Y. Zhong, T. K. Nguyen, Y. Park, T. Dinh, E. Song, R. K. Vadivelu, M. K. Masud, J. Li, M. J. A. Shiddiky, D. Dao, Y. Yamauchi, J. A. Rogers, N. T. Nguyen, Long-lived, transferred crystalline silicon carbide nanomembranes for implantable flexible electronics. *ACS Nano* **13**, 11572–11581 (2019).
47. S. Piller, M. Perrin, A. Jossen, Methods for state-of-charge determination and their applications. *J. Power Sources* **96**, 113–120 (2001).
48. Y. Xing, W. He, M. Pecht, K. L. Tsui, State of charge estimation of lithium-ion batteries using the open-circuit voltage at various ambient temperatures. *Appl. Energy* **113**, 106–115 (2014).
49. H. Rouhi, E. Karola, R. Serna-Guerrero, A. Santasalo-Aarnio, Voltage behavior in lithium-ion batteries after electrochemical discharge and its implications on the safety of recycling processes. *J. Energy Storage* **35**, 102323 (2021).
50. Y. Kurashima, T. Matsumae, H. Takagi, Room-temperature Au–Au bonding in atmospheric air using direct transferred atomically smooth Au film on electroplated patterns. *Microelectron. Eng.* **189**, 1–5 (2018).
51. Y.-H. Lee, K. W. Park, S. J. Kang, C. I. Yeo, J. B. Kim, E. K. Kang, Y. M. Song, Y. T. Lee, Fabrication and analysis of thin-film GaAs solar cell on flexible thermoplastic substrate using a low-pressure cold-welding. *Curr. Appl. Phys.* **15**, 1312–1317 (2015).
52. S. Erbel, Mechanical properties and structure of extremely strainhardened copper. *Metal. Technol.* **6**, 482–486 (1979).
53. J. Y. Lee, S. H. Park, Y. Kim, Y. U. Cho, J. Park, J. H. Hong, K. Kim, J. Shin, J. E. Ju, I. S. Min, M. Sang, H. Shin, U. J. Jeong, Y. Gao, B. Li, A. Zhumbayeva, K. Y. Kim, E. B. Hong, M. H. Nam, H. Jeon, Y. Jung, H. Cheng, I. J. Cho, K. J. Yu, Foldable three dimensional neural electrode arrays for simultaneous brain interfacing of cortical surface and intracortical multilayers. *NPJ Flex. Electron.* **6**, 86 (2022).
54. D. A. Loginova, E. A. Sergeeva, A. D. Krainov, P. D. Agrba, M. Y. Kirillin, Liquid optical phantoms mimicking spectral characteristics of laboratory mouse biotissues. *Quantum Electron.* **46**, 528–533 (2016).
55. G. Paxinos, K. B. Franklin, *Paxinos and Franklin's the Mouse Brain in Stereotaxic Coordinates* (Academic Press, 2019).
56. A. Pérez-Escudero, J. Vicente-Page, R. C. Hinz, S. Arganda, G. G. De Polavieja, idTracker: Tracking individuals in a group by automatic identification of unmarked animals. *Nat. Methods* **11**, 743–748 (2014).

Acknowledgments

Funding: This work acknowledges the support received from the National Research Foundation of Korea (grant nos. NRF-2019R1A2C2086085, , and NRF-2022M3I8A2078705), Korean government (MSIT; grant no. NRF-2022M3E5E8081196). H.C. acknowledges the support provided by NIH (award no. R21EB030140) and Penn State University. **Author contributions:** Conceptualization: J.P., K.Ki., T.S.K., I.-J.C., and K.J.Y. Device fabrication: J.P., K.Ki., C.L., and K.Ka. Solarcell fabrication: T.S.K., W.J.C., H.-B.S., and H.K.K. Mechanical simulation: B.L., Y.G., and H.C. Optical simulation: D.H.K. and Y.M.S. In vitro experiments: J.P., K.Ki., and T.S.K. In vivo experiments: J.P. and Y.K. Visualization: Y.U.C. and J.Y.L. Programminbg BLE firmware and smartphone applicaiton: J.P. and I.S.M. Writing—original draft: J.P., K.Ki., T.S.K., and Y.K. Writing—review and editing: J.P., K.Ki., T.S.K., Y.K., I.-J.C., and K.J.Y. **Competing interests:** The authors declare that they have no competing interests. **Data and materials availability:** All data needed to evaluate the conclusions in the paper are present in the paper and/or the Supplementary Materials.

Submitted 25 May 2023
Accepted 25 August 2023
Published 27 September 2023
10.1126/sciadv.adi8918